



# New nanoscale artificial pinning centres for NbTi superconductors

Tayebbeh Mousavi<sup>a,b,\*</sup>, Patrick S. Grant<sup>a</sup>, Susannah C. Speller<sup>a,b</sup>, Chris Grovenor<sup>a,b</sup>

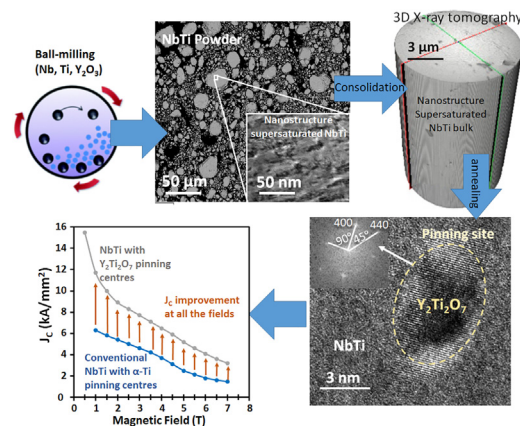
<sup>a</sup> Materials Department, Oxford University, 16 Parks Road, OX1 3PH, Oxford, UK

<sup>b</sup> Centre for Applied Superconductivity (CFAS), Materials Department, Oxford University, UK

## HIGHLIGHTS

- Superconducting NbTi bulks with improved current densities were fabricated by new processing routes.
- New artificial pinning centres of  $\text{Y}_2\text{Ti}_2\text{O}_7$  nanoparticles (<5 nm) have been developed in NbTi superconducting bulks.
- $\text{Y}_2\text{Ti}_2\text{O}_7$  nanoparticles show different pinning mechanisms from those of  $\alpha$ -Ti known as pinning centres in NbTi for many years.

## GRAPHICAL ABSTRACT



## ARTICLE INFO

### Article history:

Received 2 October 2020

Received in revised form 30 October 2020

Accepted 30 October 2020

Available online 02 November 2020

## ABSTRACT

The efficiency of new artificial pinning centres have been investigated in NbTi using the oxide dispersion strengthening (ODS) concept more typically applied to steels and Ni-superalloys. NbTi alloys containing a dispersion of nanoscale  $\text{Y}_2\text{Ti}_2\text{O}_7$  particles have been successfully manufactured through a powder metallurgy route by mechanical alloying Nb, Ti and  $\text{Y}_2\text{O}_3$  nanopowders using high energy ball milling and subsequent consolidation and annealing. The microstructure and superconducting properties of the NbTi- $\text{Y}_2\text{O}_3$  have been characterised after each processing step. After 40 h of ball milling, the  $\text{Y}_2\text{O}_3$  particles are dissolved into the nanostructured NbTi matrix formed by mechanical alloying of Nb and Ti. On annealing at temperatures above 800 °C the dissolved Y and O react with Ti from the matrix, and fine  $\text{Y}_2\text{Ti}_2\text{O}_7$  particles (<5 nm) are precipitated. These NbTi- $\text{Y}_2\text{Ti}_2\text{O}_7$  composites showed excellent superconducting performance, with  $J_c$  of  $5.2 \text{ kAmm}^{-2}$  at 4.2 K, 5 T, considerably higher than  $\text{Y}_2\text{O}_3$ -free bulks manufactured using the same process and NbTi wires manufactured using the conventional thermomechanical process. The results suggest that ODS powder processing is a promising new route to manufacture NbTi alloys containing artificial pinning centres that give superior superconducting properties.

Crown Copyright © 2020 Published by Elsevier Ltd. This is an open access article under the CC BY license (<http://creativecommons.org/licenses/by/4.0/>).

## 1. Introduction

Critical current density ( $J_c$ ) is a key parameter for applications of superconducting NbTi wires as it determines the length of wire needed to generate a given magnetic field [1] [2].  $\alpha$ -Ti (Ti-rich) precipitates have for many years been used to give effective flux pinning in these alloys [3–5], and well-established thermomechanical processing

\* Corresponding author at: Materials Department, Oxford University, 16 Parks Road, OX1 3PH, Oxford, UK.

E-mail address: [tayebbeh.mousavi@materials.ox.ac.uk](mailto:tayebbeh.mousavi@materials.ox.ac.uk) (T. Mousavi).

strategies create fine normal  $\alpha$ -Ti precipitates with an even dispersion well-matched to the spacing of magnetic flux lines under typical operating conditions [1]. However, the best  $J_c$  value achieved after careful process optimisation is  $\sim 3.2 \text{ kAmm}^{-2}$  at 5 T, 4.2 K [1], with little potential for further improvements [1,5]. The use of artificial pinning centres (APC) has been also explored in NbTi by assembling normal regions of different geometries (barrier-shaped, layer, or net-, shaped and island-shaped) within the NbTi billet, and then performing multiple extrusion stages until the desired length and diameter is achieved [6]. The materials selected for these APCs include Nb [7], Nb alloy [8], Fe [9], Ni [10] and Cu [11]. APC NbTi has some advantages over two-phase NbTi containing  $\alpha$ -Ti precipitates as it does not require such a complicated thermomechanical process and there is more freedom in the design of the number density, shape and size of the pins [7,9]. The  $J_c$  values achieved in APC NbTi composites in low fields are slightly higher than in conventional NbTi, but they are inferior at higher magnetic fields due to weak flux pinning [12]. The choice of materials for APC NbTi is also limited by the mechanical properties of the pinning material which must survive the multiple extrusion and drawing processes required to form long lengths of wire, which excludes a wide range of brittle materials from consideration as pinning centres [10] [11] [12].

In a previous study, we explored a new powder processing route to fabricate binary NbTi alloys without a casting step, and showed that the delicate two-phase microstructure required to optimise the superconducting properties can be generated by mechanical alloying and heat treatment [13]. NbTi samples were prepared from milled powder in both bulk and tape form with microstructures very similar to those in the conventional materials, and with  $J_c$  values of  $2.9 \text{ kAmm}^{-2}$  at 5 T, 4.2 K (comparable with those of conventionally processed NbTi wires). This demonstrated the potential of powder processing for producing NbTi with competitive superconducting properties, but the same process also allows us to explore a wider range of APCs beyond  $\alpha$ -Ti and ductile metals. In the work reported here, we investigate the dispersion of  $\text{Y}_2\text{O}_3$  particles into the NbTi matrix using a processing strategy based on the well-known oxide dispersion strengthening (ODS) concept used for decades in steels and Ni superalloys [14]–[17]. In these ODS materials, extensive plastic work and mechanical alloying results in the formation of metastable supersaturated solid solutions that, during a subsequent high-temperature consolidation and annealing process, results in the precipitation of oxide nanoparticles at the fine-scales required for improving the mechanical properties of structural alloys, but also suitable for pinning the flux lines in superconducting materials at high magnetic fields [16]. The efficiency of normal oxide nanoparticles as flux pinning additions has also been demonstrated recently in  $\text{Nb}_3\text{Sn}$  superconducting wires, although the process is driven by a supersaturation of oxygen [18,19] rather than a metastable supersaturation of yttrium. One variation of this process in  $\text{Nb}_3\text{Sn}$  is the addition of Zr to form oxide nanoparticles [19]. Here we show that NbTi alloys with a uniform distribution of oxide particles can be produced using a simple process by addition of the  $\text{Y}_2\text{O}_3$  particles often used in dispersion strengthened alloys [15,17,20]. The microstructure of these new NbTi composites has also been carefully characterised to provide a better understanding of how the ODS-APC concept results in significant improvements in the superconducting properties.

## 2. Experimental methods

A mixture of high-purity elemental powders of Nb (purity: 99.85%, Goodfellow), Ti (purity: 99.5%, Goodfellow) and  $\text{Y}_2\text{O}_3$  (purity: 99.999%, 20–50 nm, PI KEM Ltd) with a nominal composition of Nb-47wt%Ti-5 wt%  $\text{Y}_2\text{O}_3$  was used for the mechanical alloying process. The powder mixture and 200 stainless steel balls with a ball-to-powder weight ratio of 10:1 were sealed in a cylindrical steel pot under argon, and a Fritsch P6 planetary ball milling machine was used with rotational speed of 200 rpm at room temperature in cycles of 20-min milling followed by 15-min rest to avoid overheating the sample.

After selected milling times (10, 15, 20, 30, 40 h), 1 g samples were extracted in an Ar glove-box for characterization. The 40 h milled powder was hot-pressed into a 20 mm diameter disc using various conditions (400, 500 and 600 °C, and pressures of 40, 50 and 60 MPa) followed by annealing in evacuated quartz tubes ( $10^{-4}$  mbar) for 2 h at 700, 800 and 900 °C. The density of the bulks was measured in isopropanol using Archimedes' method.

The samples were characterised after each stage of processing. X-ray diffraction (XRD) analysis was carried out in a Rigaku Miniflex diffractometer using  $\text{Cu}_{\text{K}\alpha}$  radiation ( $\lambda = 0.154 \text{ nm}$ ) at 40 kV and 15 mA. The grain size and lattice strain were calculated from the broadening of the XRD peaks using the Williamson-Hall Eqs. [21], with instrumental broadening removed by assuming a Gaussian profile and using Nb powder with large crystallite size as a standard. Scanning Electron Microscopy (SEM) analysis was carried out using a Zeiss Merlin SEM with an Oxford Instruments (OI) 150 mm<sup>2</sup> XMax EDX detector. Transmission Electron Microscopy (TEM) was performed on a JEOL 3000F TEM, and the TEM samples were made using the ex-situ lift-out technique by Focused Ion Beam (FIB) milling.

In order to evaluate porosity and cracking in the bulk samples after sintering, 3D X-ray tomography scans were carried out using an Xradia Versa 510 micro CT system (Zeiss, Germany) operated at 100 keV energy and 7 W power (tungsten target), a voxel size of 2.47  $\mu\text{m}$  and exposure time of 8 s per projection. Each tomograph was reconstructed from 1601 projections recorded over a 360° rotation with a 4× objective and 2× binning with the 2048 × 2048 pixel CCD detector. Visualization and image processing of the tomographs were performed using Avizo 9.7.0 software (ThermoScientific, USA).

Superconducting properties were measured using a Quantum Design SQUID magnetometer and Physical Property Measurement System (PPMS). The irreversibility field ( $B_{\text{irr}}$ ) was estimated by linear extrapolation of Kramer plot with an uncertainty value of  $\pm 0.3 \text{ T}$  estimated from the fitting parameters [21]. The critical current density ( $J_c$ ) values were extracted from the full magnetic hysteresis loops using standard Bean's model [22] for cuboid samples ( $2 \times 2 \times 2 \text{ mm}$ ) cut from the consolidated pellets.

## 3. Results and discussion

### 3.1. Ball milling of powders

#### 3.1.1. Phase analysis

Fig. 1 shows the X-ray diffraction data from the NbTi- $\text{Y}_2\text{O}_3$  powder after different milling times. In the initial mixture (0 h milled), diffraction peaks of the 3 starting phases Nb, Ti and  $\text{Y}_2\text{O}_3$  can be detected. When the  $\text{Y}_2\text{O}_3$  fraction was less than 5 wt%, we were not able to detect any peaks corresponding to  $\text{Y}_2\text{O}_3$  in the initial powder suggesting that 5 wt% is just above the XRD detection limit for this combination of phases. The intensities of both Ti and  $\text{Y}_2\text{O}_3$  diffraction peaks decrease systematically with increasing milling time, and they almost disappear after 12 h. Over the same time, the Nb peaks shift significantly to smaller angles indicating that the Nb lattice is expanded. It has been shown previously [13] that ball-milling of the binary Nb–Ti system leads to the formation of  $\beta$ -Nb(Ti) alloy at room temperature after 20 h of ball-milling, but without any significant peak shift from the position of the original Nb peaks. This is because partial substitution of Nb by Ti in the bcc lattice results in almost no change in the d-spacing because Ti has a similar atomic radius to that of Nb. Therefore, the peak shift observed here in the NbTi- $\text{Y}_2\text{O}_3$  samples, coupled with the disappearance of the  $\text{Y}_2\text{O}_3$  peaks, suggest the gradual dissolution of the  $\text{Y}_2\text{O}_3$  into the  $\beta$ -Nb(Ti). During milling, brittle particles like  $\text{Y}_2\text{O}_3$  experience rapid fracture and size refinement leading to an increase in the interfacial energy of the  $\text{Y}_2\text{O}_3$  and so also of the driving force for decomposition [23]. Grain boundaries and dislocations in the ductile  $\beta$ -Nb(Ti) matrix resulting from the milling process create rapid diffusion paths that are also expected to facilitate the dissolution process. In ODS steels it has been

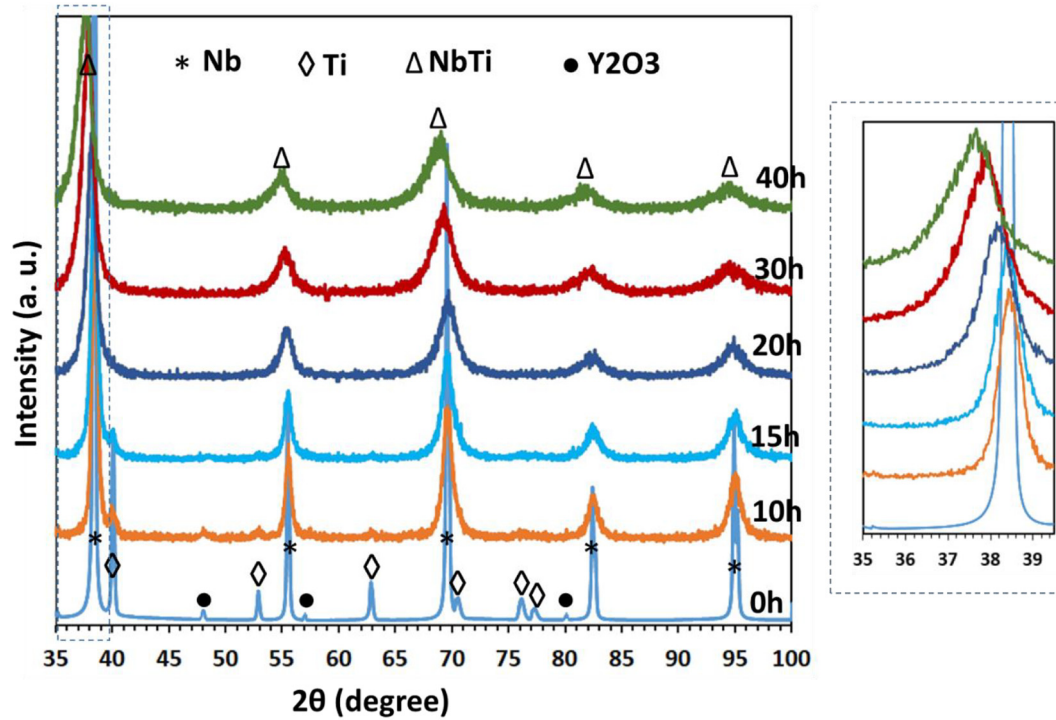


**Fig. 1.** XRD patterns of Nb-Ti-5 wt% Y<sub>2</sub>O<sub>3</sub> powder at different milling times. The insert figure is an expanded region around the (110) peak at 38.54° from the β-Nb(Ti) matrix showing the shift as a result of dissolution of yttrium and oxygen into the β-Nb(Ti).

shown that the presence of Ti promotes the dissolution of Y<sub>2</sub>O<sub>3</sub> into the bcc-Fe matrix, and also encourages the decomposition of Y<sub>2</sub>O<sub>3</sub> to separate yttrium and oxygen atoms [14,24]. Similar processes may be happening in the β-Nb(Ti) matrix in this work, with the high concentration of Ti promoting the efficient decomposition of the fine Y<sub>2</sub>O<sub>3</sub> particles.

Nb can accommodate about 5.5 at.% of oxygen in interstitial solid solution which leads to an 0.67% expansion in the lattice parameter [25]. By contrast, yttrium has been reported to have a very limited equilibrium solid-solubility in Nb (less than 0.05 at.%). However, it is well-known that ball-milling can extend the solid-solubility limits as a result of refinement of the microstructure and introduction of extremely

high concentrations of lattice defects and very large lattice strains [23,26–29]. This is the whole basis of the ODS concept since Y<sub>2</sub>O<sub>3</sub>, which has essentially no solubility in Fe or Ni even at high temperatures, has been shown to dissolve during mechanical alloying [14,24]. The atomic radius of yttrium is also larger (0.24 nm) than Nb and Ti (0.21 nm [30]), so the observed increase in lattice parameter is consistent with the dissolution of both yttrium and oxygen into the β-Nb(Ti) matrix.

In addition to the absence of Y<sub>2</sub>O<sub>3</sub> and Ti reflections and the shift of the β-Nb(Ti) peaks observed in the XRD patterns, it can be also seen that the diffraction peaks become broader at longer milling times. This peak broadening can be attributed to the well-known effects of decreasing

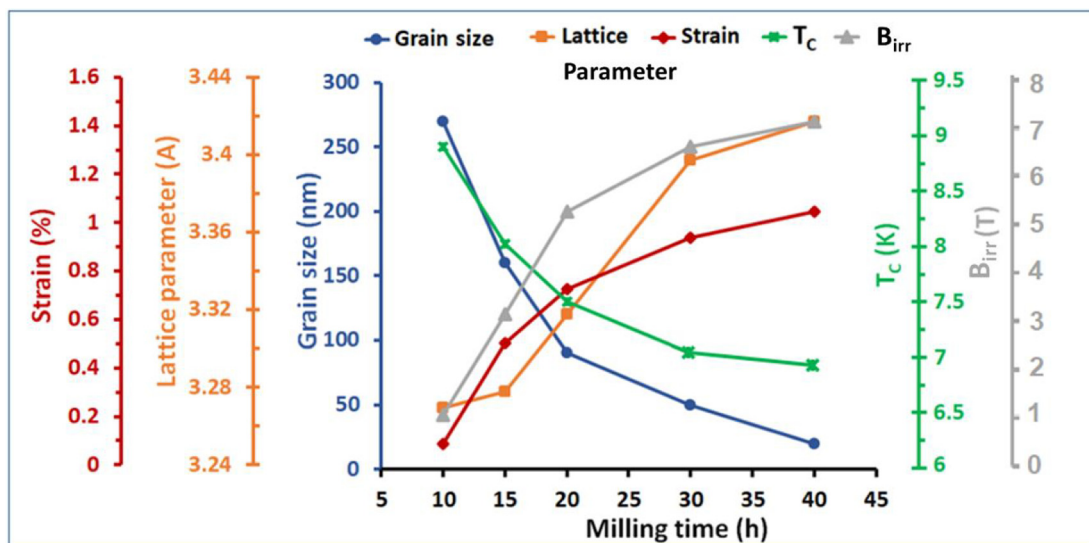


**Fig. 2.** Structural and superconducting parameters of the Nb-Ti-5 wt% Y<sub>2</sub>O<sub>3</sub> powder as a function of milling time.



crystallite size and increasing lattice strain arising from crystal defects accumulated during the cold work associated with high energy ball milling [23]. The calculated crystallite size and strains in the powder samples are presented in Fig. 2. As expected, by increasing the milling time, the crystallite size gradually decreases down to 25 nm after 40 h, while the lattice parameter is almost constant up to 15 h, and then gradually increases as the Y and O are dissolved.

The superconducting transition temperature ( $T_C$ ) and irreversibility field ( $B_{irr}$ ) values of the powder after different milling times are also presented in Fig. 2. The initial powder (milling time = 0) is a mixture of pure Nb, Ti and  $Y_2O_3$  particles, and exhibits a  $T_C$  of about 8.9 K corresponding to the value for pure Nb. The  $T_C$  value decreases with milling time to 6.9 K after 40 h of ball-milling, a much larger decrease than the 8% reduction in  $T_C$  observed previously in the ball milling of Nb–Ti without  $Y_2O_3$  [13] attributed to the additional structural disorder [31], lattice strains and impurities introduced into the powder by ball-milling. The  $B_{irr}$  value also increases as a result of the incorporation of Ti into the Nb lattice to form the  $\beta$ -Nb(Ti) alloy, but even after 40 h of ball milling the final  $B_{irr}$  value ( $\sim 7.3$  T) is lower than that of  $Y_2O_3$ -free  $\beta$ -Nb(Ti) [1]. We suppose that the observation that both the  $T_C$  and  $B_{irr}$  values obtained for the ball-milled Nb–Ti– $Y_2O_3$  powders are lower than those we previously measured in ball-milled Nb–Ti powder is due to the dissolution of yttrium and oxygen into the  $\beta$ -Nb(Ti).

### 3.1.2. Microstructure evolution

Typical SEM images from cross-sections of assemblies of NbTi– $Y_2O_3$  powder particles after different milling times are shown in Fig. 3 along with the particle size distributions. By increasing the milling time from 10 h to 40 h, the average particle size decreases and the range of the size distribution of particles increases from 5 to 60  $\mu m$  to 1–600  $\mu m$  for the Nb–Ti– $Y_2O_3$  powder. The particle size distribution of pure Nb–Ti powder (made with same initial Nb and Ti powders but without  $Y_2O_3$ ) after 40 h of ball milling is presented in Fig. 3 for comparison. In pure Nb–Ti the particle size also considerably increases to 550  $\mu m$  with a narrow size distribution, which indicates cold-welding is a dominant process during milling of these soft powders. The presence of brittle  $Y_2O_3$  particles suppresses the cold-welding and

re-welding processes during milling. In the first stages of milling, the ductile Nb and Ti particles undergo deformation and become flattened by the ball-powder-ball collisions, while brittle  $Y_2O_3$  particles undergo fragmentation. When Nb and Ti ductile particles start to weld, the brittle particles are trapped between the ductile particles, suppressing bonding and also increasing the build-up of stress, resulting in hardening and brittle fracture, all of which encourage refinement of the particle size. The impact of  $Y_2O_3$  on the microstructure of the particles can be seen in high magnification images in Fig. 3e and f. In the presence of  $Y_2O_3$ , the layered microstructure of Nb–Ti created by repeated welding of flattened Nb and Ti particles is no longer seen, and the microstructure is finer and more randomly shaped. The refinement of particle size by the addition of brittle particles like  $Y_2O_3$  has been reported in other ODS materials [23], and other ductile-brittle systems during ball-milling [32–34].

To investigate chemical variations of the ball-milled samples, EDX analysis was carried out on the Nb–Ti– $Y_2O_3$  sample after 40 h of ball milling. As seen in the back-scattered image in Fig. 4a, the sample is not chemically uniform and contains a very fine distribution of bright (Nb-rich) and dark (Ti-rich) regions. Fig. 4b shows that the yttrium content increases monotonically with the incorporation of Ti into the  $\beta$ -Nb (Ti) alloy (represented as the Ti/(Ti + Nb) ratio). It can be concluded that yttrium released by the decomposition of the  $Y_2O_3$  during ball milling is dissolved into the  $\beta$ -Nb(Ti) at roughly the same rate as the Ti is incorporated.

### 3.2. Consolidation process

Bulk samples were fabricated by pressing the 40 h-milled powder using different sintering parameters. It has been previously shown that powder-processed NbTi alloys can easily be consolidated into high density bulk samples with  $J_C$  values as high as those measured in conventional NbTi alloys [13]. Here, however, due to the hardening effects of dissolving Y and O into the NbTi, designing an effective hot pressing process is more challenging, perhaps not surprisingly given that self-welding processes were less effective during ball milling. For ball-milled NbTi powder (without  $Y_2O_3$ ), hot pressing parameters of

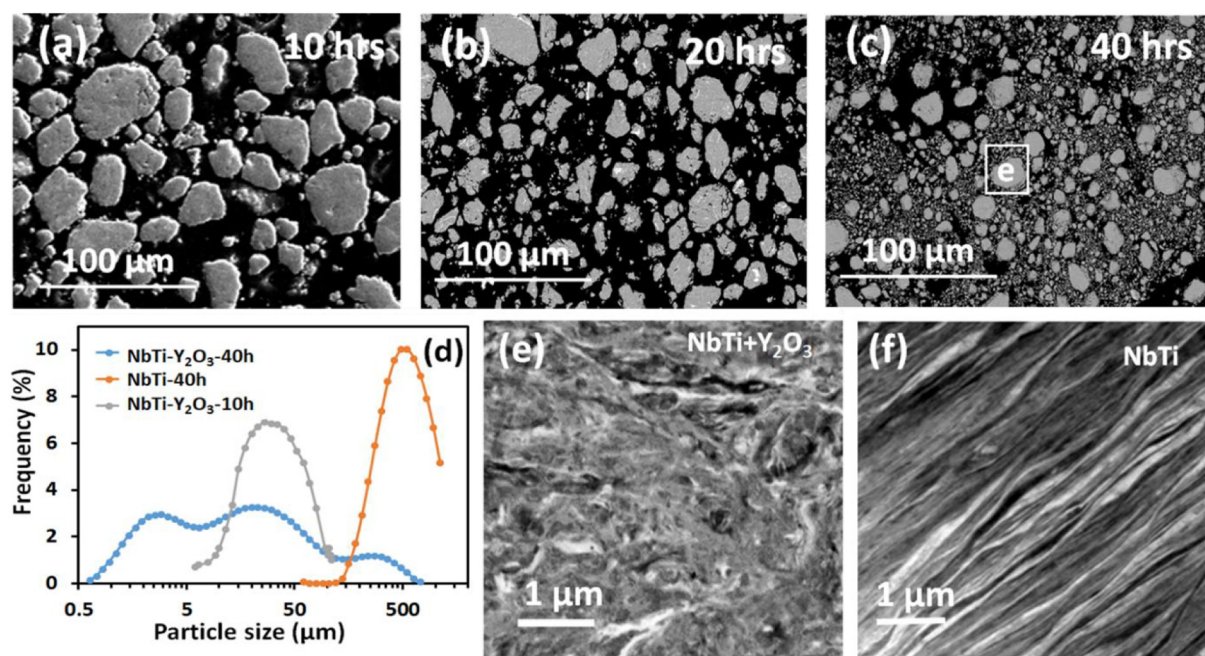
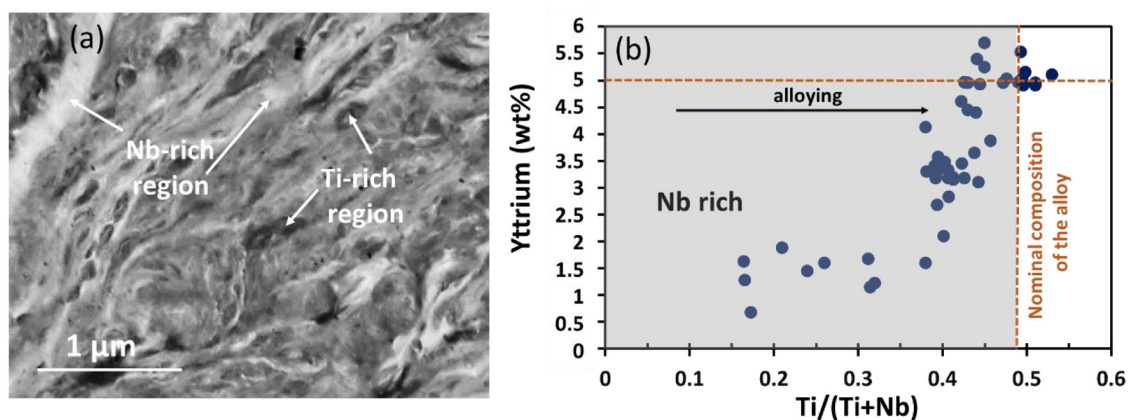


Fig. 3. (a–c) SEM images of the Nb–Ti–5wt% $Y_2O_3$  powder after different milling times, (d) Particle size distribution for the Nb–Ti–5wt% $Y_2O_3$  powder after 20 and 40 h of ball-milling and Nb–Ti powder after 40 h of ball-milling, (e and f) Back-scattered SEM image of a 40 h-milled Nb–Ti–5wt% $Y_2O_3$  powder particle and a 40 h-milled Nb–Ti powder particle respectively.



**Fig. 4.** (a) SEM Back-scattered image of the Nb-Ti-Y<sub>2</sub>O<sub>3</sub> sample after 40 h of ball milling, (b) Yttrium content as a function of Ti/(Nb + Ti) weight ratio for the Nb-Ti-Y<sub>2</sub>O<sub>3</sub> sample after 40 h of ball milling. This chemical analysis has been performed on a thin TEM sample with a thickness less than 80 nm for better spatial resolutions. Each data point is a point analysis on a random area through a series of different images across the sample. The error bar of the data points is  $\pm 0.02$ . The dashed line corresponds to the initial average values in the starting powder mixture.

400 °C–40 MPa lead to a high relative density of 97.6% [13]. For NbTi-Y<sub>2</sub>O<sub>3</sub>, a range of higher temperatures was chosen considering the need to avoid excessively high temperatures to minimise coarsening of the fine microstructure produced in the as-milled powder. The relative density of the NbTi-Y<sub>2</sub>O<sub>3</sub> bulk samples hot pressed at various temperatures and pressures are presented in Fig. 5a. As expected, increasing either pressure or temperature improves the relative density, but pressure has the strongest effect. For example, the relative density of the pellets improves from 77.2% to 95% when the pressure is increased from 40 MPa to 60 MPa at a constant temperature of 500 °C, while the density only improves from 77.2 to 83% when the temperature is increased from 400 to 600 °C at a pressure of 50 MPa.

To investigate porosity and cracking of these samples in 3D, X-ray tomography scans of cylindrical specimens were taken with the axial direction parallel to the pressing direction. Cross-sectional tomography images from the top, middle and bottom of each cylinder are shown in Fig. 5b. Since the tomography technique is non-destructive, the pores and cracks identified in these images are not a result of any polishing process. For the sample sintered at high temperature and low pressure (600 °C, 40 MPa), numerous coarse randomly-shaped 1–5  $\mu$ m pores can be observed. In contrast, the sample processed at high pressure and high temperature (600 °C, 60 MPa) has a very dense microstructure with hardly any porosity, but includes relatively large features that might be a result of coarsening. A large crack growing along the boundaries of these larger features and perpendicular to the pressure axis can be also seen at the bottom end of the cylinder, perhaps as a result of thermal contraction stresses during cooling. When the sample is hot pressed at a moderate temperature and high pressure (500 °C, 60 MPa), no obvious porosity or cracks can be detected in the tomography data, and the microstructure looks finer compared to the sample processed at 600 °C. The reduction in porosity with increasing pressure observed in the tomography data is in good agreement with the density measurements presented in Fig. 5a. It can be concluded that the hot pressing process can be divided into two stages; densification without obvious coarsening up to 500 °C, and coarsening without much further densification and cracking at higher temperatures. Using processing conditions of 500 °C and a pressure of 60 MPa, NbTi-Y<sub>2</sub>O<sub>3</sub> bulks with a relative density as high as 95% could be obtained.

### 3.3. Annealing studies

It was shown that after 40 h of ball milling the Y<sub>2</sub>O<sub>3</sub> is dissolved into the  $\beta$ -Nb(Ti) alloy, reducing both  $T_C$  and  $B_{irr}$ . If we are to reproduce the ODS concept in these materials, the supersaturation of dissolved Y and O

from the mechanical alloying should precipitate out during a subsequent annealing process in these samples. In order to encourage precipitation of Y in metastable solid solution, subsequent annealing process was carried out on the consolidated bulk samples at temperatures between 700 and 900 °C, and the phase distribution in these sample compared by XRD analysis, Fig. 6. The XRD pattern from the as-pressed sample shows the NbTi peaks are slightly shifted to higher angles compared to the as-milled sample, but are still in the lower angles compared to the annealed samples. These results suggest that during consolidation at 500 °C the dissolved Y and O do not precipitate out fully from the  $\beta$ -Nb(Ti) matrix, but some is still in solid solution. As a result, the improvements in the superconducting properties ( $T_C = 7.5$  K and  $B_{irr} = 8.3$  T) are not significant for the as-pressed sample. The XRD data from the sample annealed at 700 °C shows only peaks corresponding to  $\beta$ -Nb(Ti) but now clearly shifted towards higher angles, suggesting that the metastable solution of Y and O impurities are removed from the lattice. As the annealing temperature is increased to 800 and 900 °C, the positions of the NbTi peaks are unchanged but the peaks become narrower and stronger due to the release of internal strain induced by high energy ball-milling, coarsening of the microstructure and possibly better uniformity in composition. No sign of any other secondary phases could be detected in these XRD results suggesting that impurity atoms leaving the  $\beta$ -Nb(Ti) matrix form either amorphous or very small crystalline clusters which cannot be detected. According to the Nb-Ti phase diagram, the  $\alpha$ -Ti precipitate which is a common secondary phase in conventional Nb-Ti alloys, is only formed below  $\sim 400$  °C [35], and hence is not expected to be present in the samples in this work as both the consolidation and annealing temperatures are all above 400 °C.

TEM analysis was performed in order to examine the microstructure of the annealed samples in more detail. As can be seen in Fig. 7, there are fine-scale particles ( $< 5$  nm) distributed throughout the matrix for the samples annealed at 800 and 900 °C. The crystal structure of these dispersed particles was examined by high-resolution TEM lattice imaging. To identify the crystal structure of the particles, two different  $d$  spacing values (for two sets of planes) and the angle between these planes were obtained from Fast Fourier Transforms (FFT) of the oxide particles and compared with database values for possible phases including Y<sub>2</sub>O<sub>3</sub>, Y<sub>2</sub>TiO<sub>5</sub> and Y<sub>2</sub>Ti<sub>2</sub>O<sub>7</sub>. For the sample annealed at 800 °C the analysis of the particle in Fig. 7b matches the [001] zone of the cubic Y<sub>2</sub>Ti<sub>2</sub>O<sub>7</sub> structure (JCPDS: 42-0413). In this sample, 8 particles were analysed, and they could all be identified as fcc Y<sub>2</sub>Ti<sub>2</sub>O<sub>7</sub> with particle sizes ranging from 2 to 5 nm. Similar analysis of the microstructure of the sample annealed at 900 °C is presented in Fig. 7(c) and (d), and 6 particles in this sample were also all identified to be fcc Y<sub>2</sub>Ti<sub>2</sub>O<sub>7</sub>. These observations

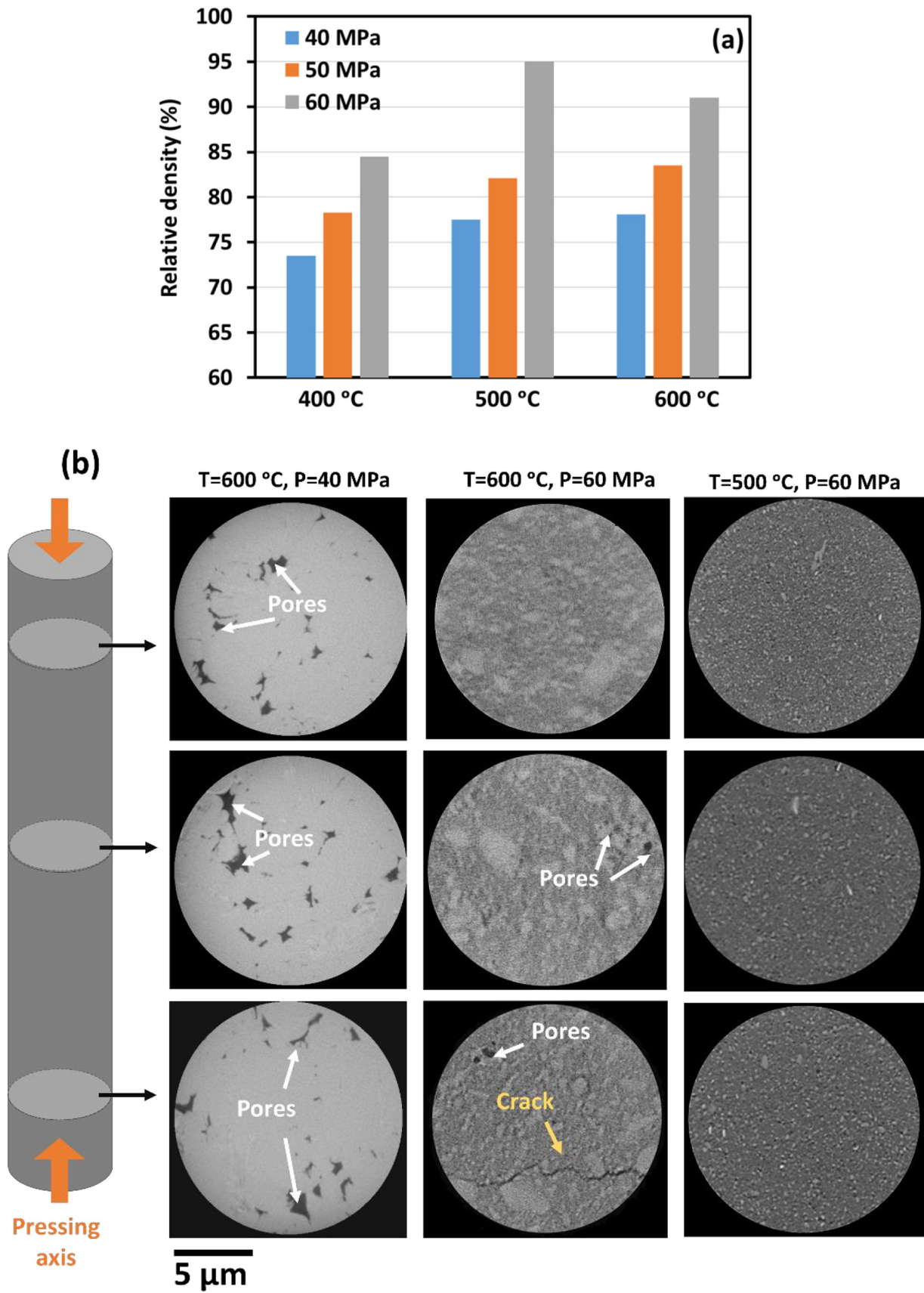


**Fig. 5.** (a) Relative densities of NbTi-Y<sub>2</sub>O<sub>3</sub> pellets hot pressed at various temperatures and pressures. (b) X-ray tomography images from NbTi-Y<sub>2</sub>O<sub>3</sub> bulk samples prepared under different pressing parameters.



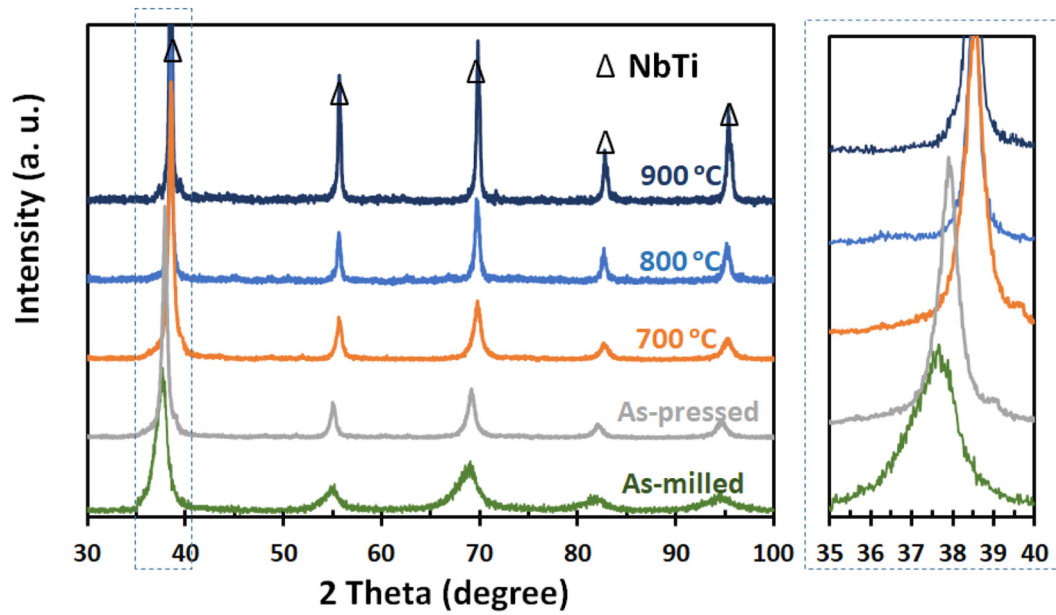


**Fig. 6.** XRD patterns of the NbTi-Y<sub>2</sub>O<sub>3</sub> samples after consolidation at 500 °C and 60 MPa and also after annealing at different temperatures. The insert figure shows the peak shift around the (110) NbTi peak at 38.54°.

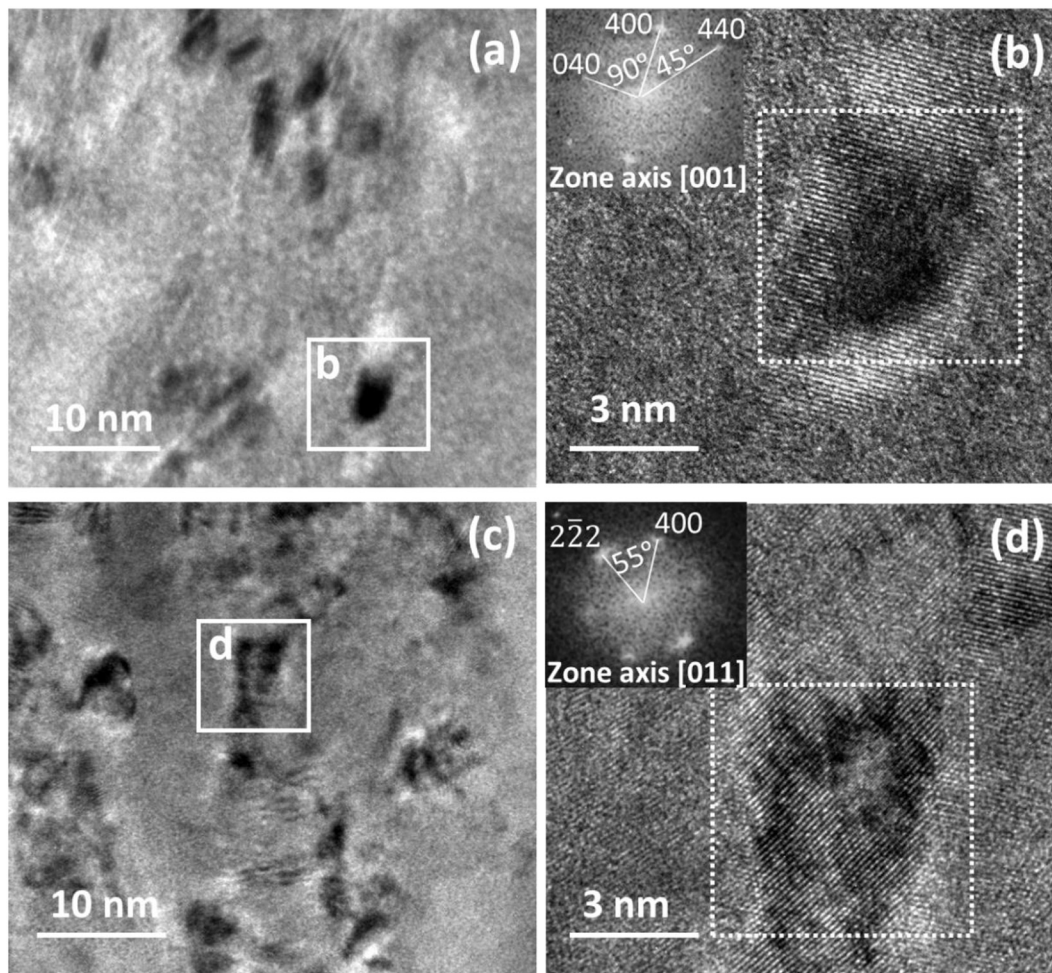


**Fig. 7.** High resolution TEM images of the NbTi-Y<sub>2</sub>O<sub>3</sub> bulk samples after annealing at (a,b) 800 °C and (c,d) 900 °C. In (b) the interplanar spacings 2.57, 2.53 and 1.77 Å, and the inter-axial angles are determined to be 90.1, 44.7 and 45.0°. These results agree well with the (400), (040) and (440) planes of fcc Y<sub>2</sub>Ti<sub>2</sub>O<sub>7</sub> lattice (JCPDS: 42-0413). In (d) two sets of d spacings 2.9 Å and 2.41 Å are identified with an angle of 55°, corresponding to the (222) and (400) planes of fcc Y<sub>2</sub>Ti<sub>2</sub>O<sub>7</sub> respectively. The zone axis of the FFT in Fig. 7b is identified as [011].

**Table 1**

Superconducting properties of the NbTi-Y<sub>2</sub>O<sub>3</sub> after 40 h of ball milling followed by pressing and annealing at different temperatures. J<sub>c</sub> values were extracted from the full magnetic hysteresis loops using Bean's model.

	T <sub>c</sub> (K)	B <sub>irr</sub> (T) (at 4.2 K)	J <sub>c</sub> (kAmm <sup>-2</sup> ) at (4.2 K, 5 T)
NbTi-Y <sub>2</sub> O <sub>3</sub> (40 h-milled)	6.9	7.2	–
NbTi- Y <sub>2</sub> O <sub>3</sub> (Pressed at 500 °C, 60 MPa)	7.5	8.3	1.01
NbTi- Y <sub>2</sub> O <sub>3</sub> (annealed at 700 °C)	8.9	9.8	1.02
NbTi- Y <sub>2</sub> O <sub>3</sub> (annealed at 800 °C)	8.9	10.4	5.01
NbTi- Y <sub>2</sub> O <sub>3</sub> (annealed at 900 °C)	8.9	10.5	5.20
NbTi- Y <sub>2</sub> O <sub>3</sub> (annealed at 900 °C, 350 °C)	8.9	10.5	5.45
Commercial NbTi [1]	9.2	11	3.20

show that after annealing above 800 °C in the presence of an excess of Ti the dissolved Y and O preferentially form Y<sub>2</sub>Ti<sub>2</sub>O<sub>7</sub> which is the most thermodynamically stable of the possible Y<sub>2</sub>O<sub>3</sub>, Y<sub>2</sub>TiO<sub>5</sub> and Y<sub>2</sub>Ti<sub>2</sub>O<sub>7</sub> phases [36].

Similar results on the formation of Y<sub>2</sub>Ti<sub>2</sub>O<sub>7</sub> have been reported for ODS ferritic steels processed with Y<sub>2</sub>O<sub>3</sub> particles when Ti is also present [14,24,37], but in the absence of Ti, reformation of Y<sub>2</sub>O<sub>3</sub> precipitates has been observed [14,24]. In this work, no Y<sub>2</sub>Ti<sub>2</sub>O<sub>7</sub> particles were detected in the sample annealed at 700 °C, which is consistent with results on ODS steels where the crystallization temperature for the Y<sub>2</sub>Ti<sub>2</sub>O<sub>7</sub> phase was reported to be around 800 °C [37]. Increasing the annealing temperature to 900 °C resulted in no measurable coarsening of the Y<sub>2</sub>Ti<sub>2</sub>O<sub>7</sub> particles (Fig. 7c). The size stability of these oxides at high temperatures has also been observed in ferritic alloys [37], and so the Y<sub>2</sub>Ti<sub>2</sub>O<sub>7</sub> particles described here show a much higher resistance to coarsening at high temperature than the α-Ti precipitates that are common pinning sites in NbTi alloys [1]. This is important for the superconducting properties as the particles need to be kept small enough to act as effective pinning centres.

### 3.4. Superconducting properties

Table 1 and Fig. 8 summarise the superconducting properties extracted from magnetisation-temperature (M-T) curves and magnetic

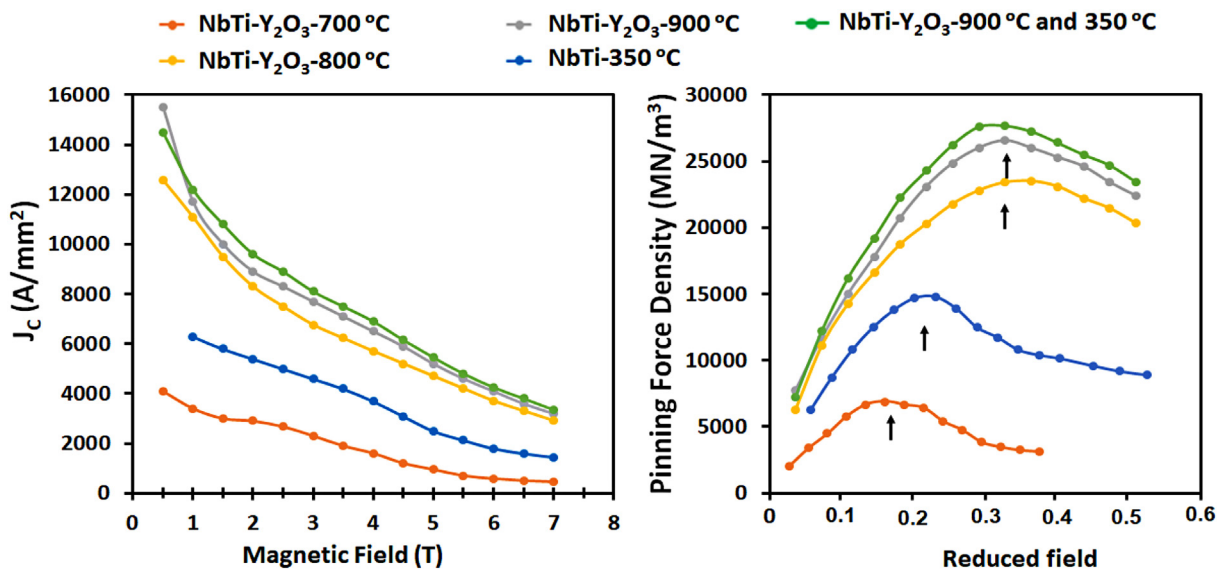
hysteresis loops on the hot pressed NbTi-Y<sub>2</sub>O<sub>3</sub> samples after consolidation and annealing at different temperatures. Compared with the values from the 40 h milled powder, the T<sub>c</sub> and B<sub>irr</sub> values improve to 8.9 K and 10 T respectively when annealed at 700 °C, with no further change at higher annealing temperatures. These T<sub>c</sub> and B<sub>irr</sub> values are considerably higher than those of the 40 h-milled powder due to the fact that the dissolved Y and O have precipitated out from the NbTi matrix during annealing as well as the release of strain and improvement in structural order. These values are comparable with the T<sub>c</sub> and B<sub>irr</sub> values of the commercial NbTi processed by conventional techniques [1].

Fig. 8 shows magnetisation J<sub>c</sub> values and pinning force densities measured as a function of magnetic field for the NbTi-Y<sub>2</sub>O<sub>3</sub> samples annealed at different temperatures. For comparison, the J<sub>c</sub> data of a NbTi bulk sample with no Y<sub>2</sub>O<sub>3</sub> processed in a similar way but heat treated to contain Ti precipitates as pinning centres [13] has been included. Annealing the NbTi-Y<sub>2</sub>O<sub>3</sub> samples at 800 °C or 900 °C to give a dispersion of Y<sub>2</sub>Ti<sub>2</sub>O<sub>7</sub> nanoparticles as shown above, leads to an enhancement in both J<sub>c</sub> and pinning force density relative to the pure NbTi containing Ti precipitates. However, annealing at the lower temperature of 700 °C results in dramatically lower J<sub>c</sub> and pinning force density values.

To analyse flux pinning mechanisms in these NbTi-Y<sub>2</sub>O<sub>3</sub> samples, the Dew-Hughes model and multi-elementary scaling modelling was employed [38]. According to the Dew-Hughes model [38], core pinning sites can arise from two phenomena, 'Δκ pinning' resulting from small differences in the Ginzburg parameter due to composition fluctuations, and 'normal pinning' resulting from non-superconducting particles such as normal phases and defects. Depending on the size of the pinning centres compared to the inter flux line spacing (*d*), the pinning sites can be defined as point, surface or volume pins. Point sites are regions with all dimensions less than *d*, surface sites have two dimensions greater than *d* and volume sites have all dimensions larger than *d*. Therefore, in the Dew-Hughes model, there are six pinning functions describing the pinning parameters defined using the following equation:

$$F_p = Ab^p(1-b)^q \quad (1)$$

where (*b* = *B*/*B*<sub>irr</sub>), *F<sub>p</sub>* is the pinning force density, *A* is a parameter associated with the pinning strength and *p* and *q* are parameters



**Fig. 8.** (a) J<sub>c</sub> and (b) pinning force density as a function of magnetic field and reduced field (*B*/*B*<sub>irr</sub>) respectively at 4.2 K for the NbTi-Y<sub>2</sub>O<sub>3</sub> pellets after annealing at various temperatures. The data in blue represents the values for the NbTi pellet which has been processed by a similar ball milling procedure but annealing at a lower temperature to create a microstructure including α-Ti precipitates as pinning sites within the NbTi matrix. (For interpretation of the references to colour in this figure legend, the reader is referred to the web version of this article.)



describing the actual pinning mechanism. The theoretical values of  $p$  and  $q$  and the position of the peak maximum in the  $Fp$ - $b$  plot depend on the geometry (point, surface and volume) and the type (normal or  $\Delta\kappa$ ) of the active pinning sites [38].

By fitting a curve to the experimental data,  $p$  and  $q$  values can be evaluated and the active pinning mechanisms can be identified. However, there may exist several active pinning mechanisms simultaneously with different contributions to the overall flux pinning. It is therefore more precise to consider more than one mechanism and give each of them a weighting parameter in the equation of the fitted curve. The weighting parameters which show the contribution of each mechanism can be determined by fitting a curve to the above equation. For this work, a good fit to the experimental pinning curves was obtained when a combination of volume and surface normal pinning is considered. Details on how these calculations were performed can be found in supplementary appendix. This method has been applied by other groups [39–42].

Using these models, it was found that the dominant pinning mechanism for the samples annealed at various temperatures is different. For the samples annealed at 800 °C and 900 °C, volume normal pinning is the dominant mechanism, with a small contribution of surface normal pinning. However, for the sample annealed at 700 °C surface normal pinning is the dominant mechanism. The dominant mechanism for the pure NbTi was also found to be surface normal, with 25% contribution from volume normal pinning. This change in dominant pinning mechanism from surface to volume normal pinning leads to a shift in the pinning force density peak position towards higher reduced magnetic fields ( $b$ ) for the samples annealed at 800 and 900 °C, as seen in Fig. 8b. It was supposed that this difference in mechanism suggests that the  $Y_2Ti_2O_7$  nanoparticles that result in volume normal pinning are not formed in the sample annealed at 700 °C. The pure ball-milled NbTi described in a previous work [13] includes precipitates of  $\alpha$ -Ti with a size of about 3–8 nm, slightly larger than the Y-Ti-O precipitates in this work, leading to the introduction of 25% contribution from volume normal pinning in addition to the dominant surface normal pinning. It is worth mentioning that to create this two phase microstructure this sample is annealed at a much lower temperature (350 °C) to lie in the two-phase region ( $\alpha$ -Ti +  $\beta$ -NbTi) in the Nb–Ti phase diagram [35]. In the NbTi- $Y_2O_3$  samples, the annealing temperature needs to be higher to encourage precipitation of the oxide particles, and the matrix therefore lies within the single phase ( $\beta$ -NbTi) region of the Nb–Ti phase diagram. In order to explore the benefit of generating these  $\alpha$ -Ti precipitates in addition to the  $Y_2Ti_2O_7$  particles, the NbTi- $Y_2O_3$  sample annealed at 900 °C was then annealed again at 350 °C. This second annealing is expected to make no difference to the  $Y_2Ti_2O_7$  particles formed at a much higher temperature, but would create the  $\alpha$ -Ti precipitates throughout the matrix as confirmed previously [13]. The  $J_c$  data from this ‘doubly pinned’ sample shown in Fig. 8 is slightly higher than the NbTi- $Y_2O_3$  annealed at 900 °C over almost the whole field range studied, presumably as a result of the introduction of these new pinning centres. The pinning force density analysis (Fig. 8b) for the samples with only either  $\alpha$ -Ti precipitates (the blue line) or  $Y_2Ti_2O_7$  particles (the grey line) shows that the oxide particles are stronger and more effective pinning centres possibly due to their size, shape and reduced interparticle spacing, but that a combination of both kinds of pinning site results in an even higher pinning force. This suggests that there are other materials which can be more effective pinning sources than the  $\alpha$ -Ti precipitates for NbTi superconductors, and the ODS technique can be successful for fabricating nano-scale distributions of these artificial pinning centres.

#### 4. Conclusions

Superconducting NbTi bulks with new artificial pinning centres of  $Y_2Ti_2O_7$  were successfully manufactured following the ODS concept using high energy ball milling of Nb, Ti and  $Y_2O_3$  powders. A NbTi

alloy is formed during mechanical alloying and the thermodynamically stable  $Y_2O_3$  particles decompose and yttrium and oxygen dissolve into a metastable solid solution in the NbTi matrix. The milled powder showed significant residual strain and fine crystallite size (~30 nm), and degraded  $T_c$  and  $B_{irr}$  values. The sintering process at moderate temperature and high pressure leads to bulk pellets with density as high as 95.5%. Subsequent annealing above 800 °C leads to the dissolved Y and O reacting with Ti and precipitating out of the matrix as fine-scale particles (<5 nm) of the thermodynamically stable  $Y_2Ti_2O_7$  phase. These  $Y_2Ti_2O_7$  particles act as effective flux pinning sites and significantly improve the  $J_c$  value of NbTi bulk samples up to 5.2 kAmm<sup>-2</sup> at 4.2 K and 5 T. This work shows the high potential of powder processing and the ODS concept to introduce new materials as artificial pinning centres into NbTi which are highly effective in the enhancement of the critical current density.

#### CRediT authorship contribution statement

**Tayebeh Mousavi:** Conceptualization, Methodology, Writing - original draft, Visualization, Investigation, Data curation. **Patrick S. Grant:** Funding acquisition and processing methodology. **Susie Speller:** Supervision, Validation, Funding acquisition. **Chris Grovenor:** Conceptualization, Supervision, Validation, Funding acquisition.

#### Declaration of Competing Interest

The authors declare that they have no known competing financial interests or personal relationships that could have appeared to influence the work reported in this paper.

#### Acknowledgments

We acknowledge the funding provided by Centre for Applied Superconductivity at University of Oxford, and UK Engineering and Physical Sciences Research Council grant EP/P006566/1.

#### Appendix A. Supplementary data

Supplementary data to this article can be found online at <https://doi.org/10.1016/j.matdes.2020.109285>.

#### References

- [1] P.J. Lee, *Abridged Metallurgy of Ductile Alloy Superconductors*, Wiley Encycl. Electr. Electron. Eng., 1999.
- [2] J.F. Li, P.X. Zhang, X.H. Liu, J.S. Li, Y. Feng, S.J. Du, T.C. Wang, W.T. Liu, G. Grunblatt, C. Verwaerde, G.K. Hoang, The microstructure of NbTi superconducting composite wire for ITER project, *Phys C Supercond* 468 (15) (2008) 1840–1842.
- [3] D.C. Larbalestier, P.J. Lee, New development in NbTi superconductors, *Proc Part Accel Conf Dallas TX USA 2* (1995) 1276–1281, <https://doi.org/10.1109/PAC.1995.505199>.
- [4] R.W. Heussner, Magnetization critical current density of conventional and artificial pinning center (APC) NbTi superconducting wires, *J Magn Magn Mater* 230 (2001) 298–300.
- [5] P.J. Lee, D.C. Larbalestier, Determination of the flux pinning force of Ti ribbons in Nb46.5wt% Ti produced by heat treatments of varying temperature, duration and frequency, *J Mater Sci* 23 (11) (1988) 3951–3957.
- [6] X.H. Liu, Y. Feng, A. Sulpice, R. Tournier, E. Mossang, Superconducting properties of Nb50Ti/Cu superconducting composites with different forms of artificial pinning centre, *Phys C Supercond* 396 (2003) 1048–1052.
- [7] O. Miura, K. Matsumoto, Y. Tanaka, K. Yamafuji, M. Iwakuma, K. Funaki, T. Matsushita, Pinning characteristics in multifilamentary Nb-Ti superconducting wires with sub-micrometre filaments introduced artificial pinning centres, *Cryogenics* 32 (3) (1992) 315–322.
- [8] D. Heussner, R.W. Bormio-Nunes, C.E. Cooley, L.D. Larbalestier, Artificial pinning center Nb-Ti superconductors with alloyed Nb pins, *IEEE Trans Appl Supercond* 7 (2) (1997) 1142.
- [9] L.D. Larbalestier, P. Cooley, W. Jablonski, D. Heussner, Nb-Ti composite wires with artificial ferromagnetic pins, *Adv Cryog Eng Mater* 42 (1996) 1095.
- [10] J.Q. Zeitlin, A. Wang, B. Motowidlo, N.D. Rizzo, J.D. McCambridge, L.R. Prober, Ferromagnetic artificial pinning centers in multifilamentary superconducting wires, *Adv Cryog Eng Mater* 42 (1996) 1109.

- [11] H. Motowidlo, L.R.A. Zeitlin, B.A.A. Walker, Multifilament NbTi with artificial pinning centers: the effect of alloy and pin material on the superconducting properties, *Appl Phys Lett* 61 (8) (1992) 991.
- [12] R.W. Heussner, P.J. Bormio Nunes, P.J. Lee, D.C. Larbalestier, Properties of niobium-titanium superconducting wires with Nb artificial pinning centers, *J Appl Phys* 80 (1996) 1640.
- [13] T. Mousavi, Z. Hong, A. Morrison, A. London, P.S. Grant, C. Grovenor, S. Speller, A new approach to fabricate superconducting NbTi alloys, *Supercond Sci Technol* 30 (9) (2017) 094001.
- [14] A.J. London, S. Santra, S. Amirthapandian, B.K. Panigrahi, R.M. Sarguna, Effect of Ti and Cr on dispersion, structure and composition of oxide nano-particles in model ODS alloys, *Acta Mater* 97 (2015) 223.
- [15] T. Liu, H. Shen, C. Wang, W. Chou, Progress in natural science: materials international structure evolution of  $Y_2O_3$  nanoparticle/Fe composite during mechanical milling and annealing, *Prog Nat Sci Mater Int* 23 (4) (2013) 434–439.
- [16] H. Zhang, M.J. Gorley, K. Boon, M.E. Fitzpatrick, S.G. Roberts, P.S. Grant, An in situ powder neutron diffraction study of nano-precipitate formation during processing of oxide-dispersion-strengthened ferritic steels, *J Alloys Compd* 582 (2014) 769–773.
- [17] L. Zhang, S. Ukai, T. Hoshino, S. Hayashi, X. Qu,  $Y_2O_3$  evolution and dispersion refinement in co-base ODS alloys, *Acta Mater* 57 (12) (2009) 3671–3682.
- [18] X. Xu, J. Rochester, X. Peng, M. Sumption, M. Tomsic, Ternary Nb3Sn superconductors with artificial pinning centers and high upper critical fields, *Supercond Sci Technol* 32 (2) (2019) 02LT01.
- [19] L.R. Motowidlo, P.J. Lee, C. Tarantini, S. Balachandran, A.K. Ghosh, D.C. Larbalestier, An intermetallic powder-in-tube approach to increased flux-pinning in Nb3Sn by internal oxidation of Zr, *Supercond Sci Technol* 31 (1) (2017) 014002.
- [20] I. Hilger, M. Tegel, M.J. Gorley, P.S. Grant, T. Weißgärber, B. Kieback, The structural changes of  $Y_2O_3$  in ferritic ODS alloys during milling, *J Nucl Mater* 447 (1–3) (2014) 242–247.
- [21] E.J. Kramer, Scaling laws for flux pinning in hard superconductors, *J Appl Phys* 44 (1973) 1360.
- [22] G.K. Williamson, W.H. Hall, X-ray line broadening from filed aluminium and wolfram, *Acta Metall* 1 (1) (1953) 22–31.
- [23] C. Suryanarayana, Mechanical alloying and milling, *Prog Mater Sci* 46 (1–2) (2001) 1–184.
- [24] T. Liu, L. Wang, C. Wang, H. Shen, H. Zhang, Feasibility of using  $Y_2Ti_2O_7$  nanoparticles to fabricate high strength oxide dispersion strengthened Fe–Cr–Al steels, *JMADE* 88 (2015) 862–870.
- [25] N.J. Doyle, A. Taylor, Solid solubility limits of Y and Sc in the W, Nb and Cr, *J Less Common Metals* 9 (3) (1965) 214–232.
- [26] S. Sabooni, T. Mousavi, F. Karimzadeh, Thermodynamic analysis and characterisation of nanostructured Cu(Mo) compounds prepared by mechanical alloying and subsequent sintering, *Powder Metall* 55 (3) (2012) 222.
- [27] T. Mousavi, F. Karimzadeh, M.H. Abbasi, Synthesis and characterization of nanocrystalline NiTi intermetallic by mechanical alloying, *Mater Sci Eng A* 487 (1–2) (2008) 46–51.
- [28] S.N. Hosseini, T. Mousavi, F. Karimzadeh, M.H. Enayati, Thermodynamic aspects of nanostructured CoAl intermetallic compound during mechanical alloying, *J Mater Sci Technol* 27 (7) (2011) 601–606.
- [29] T. Mousavi, M.H. Abbasi, F. Karimzadeh, Thermodynamic analysis of NiTi formation by mechanical alloying, *Mater Lett* 63 (9–10) (2009) 786–788.
- [30] J.C. Slater, Atomic radii in crystals, *J Chem Phys* 41 (1964) 3199.
- [31] R.A. Webb, Noise thermometry at ultralow temperatures, *J Low Temp Phys* 13 (3/4) (1973) 383–429.
- [32] T. Mousavi, F. Karimzadeh, M.H. Abbasi, Mechanochemical assisted synthesis of NiTi intermetallic based nanocomposite reinforced by  $Al_2O_3$ , *J Alloys Compd* 467 (2009) 173.
- [33] T. Mousavi, F. Karimzadeh, M.H. Abbasi, M.H. Enayati, Investigation of Ni nanocrystallization and the effect of  $Al_2O_3$  addition by high-energy ball milling, *J Mater Process Technol* 204 (1) (2008) 125–129.
- [34] S. Sabooni, T. Mousavi, F. Karimzadeh, Mechanochemical assisted synthesis of Cu (Mo)/ $Al_2O_3$  nanocomposite, *J Alloys Compd* 497 (2010) 95.
- [35] A.K. Mallik, Computer calculations of phase diagrams, *Bull Mater Sci* 8 (2) (1986) 107–121.
- [36] Y. Jiang, J.R. Smith, G. Robert Odette, Prediction of structural, electronic and elastic properties of  $Y_2Ti_2O_7$  and  $Y_2TiO_5$ , *Acta Mater* 58 (5) (2010) 1536–1543.
- [37] J. Macías-delgado, T. Leguey, V. De Castro, M.A. Auger, M.A. Monge, P. Spätig, Microstructure and tensile properties of ODS ferritic steels mechanically alloyed with  $Fe_2Y$ , *Nucl Mater Energy* 9 (2016) 372–377.
- [38] D. Dew-Hughes, Flux pinning mechanisms in type II superconductors, *Philos Mag* 30 (2) (1974) 293–305.
- [39] T. Mousavi, C. Aksoy, C.R.M. Grovenor, S.C. Speller, Microstructure and superconducting properties of Sn – In and Sn – In – Bi alloys as Pb-free superconducting solders, *Supercond Sci Technol* 29 (1) (2015) 015012.
- [40] D. Patel, M.S. Al Hossain, K.W. See, W. Qiu, H. Kobayashi, Z. Ma, S.J. Kim, J. Hong, J.Y. Park, S. Choi, M. Maeda, M. Shahabuddin, M. Rindfleisch, M. Tomsic, S.X. Dou, J.H. Kim, Evaluation of persistent-mode operation in a superconducting  $MgB_2$  coil in solid nitrogen, *Supercond Sci Technol* 29 (4) (2016) 04LT02.
- [41] T. Mousavi, S. Speller, C. Grovenor, Structural parameters affecting superconductivity in iron chalcogenides: review, *Mater Sci Technol* 30 (15) (2014) 1929–1943.
- [42] T. Kawabata, T. Namiki, K. Matsuda, D. Tokai, S. Murakami, K. Nishimura, Superconductivity of  $MgB_2$  composited with Mg–Zn alloys, *Arch Metall Mater* 58 (2) (2013) 1–4.